Defects in wetting fronts: Experimental and theoretical results

O. Zik,[1] T. Kustanovich,[2] E. Moses,[1] and Z. Olami[2]
[1]*Department of Physics of Complex Systems, The Weizmann Institute of Science, Rehovot 76100, Israel*
[2]*Department of Chemical Physics, The Weizmann Institute of Science, Rehovot 76100, Israel*
(Received 28 August 1997; revised manuscript received 13 March 1998)

We study flow in a porous medium in the presence of a discontinuous perturbation (defect) that perturbs its parameters. The discontinuous perturbation is at the interface between regions of different porosities, produced in the experiment by uniformly depositing black toner with a laser printer. When water propagates in such a medium the wetting front develops a nontrivial, curved steady state solution. We present experimental measurements of the profiles and their propagation rate, as well as the characteristics of the steady state solution. A naive attempt to use perturbation theory fails due to discontinuities at the ''defect.'' We proceed to develop a theoretical treatment based on Laplacian flow, that is good to all orders and predicts most of the features that can be observed. We find good quantitative agreement between theory and experiment, without any fit parameters. [S1063-651X(98)14706-2]

PACS number(s): 47.55.Mh, 47.15.Hg, 68.45.Gd

I. INTRODUCTION

The role of ''defects'' in nonequilibrium systems is an intriguing question that has recently received much attention. Defects are a spatial manifestation of singularities in the order parameter, and as such they teach us both about the order parameter and about the medium itself. In *equilibrium* systems the role of imperfections and impurities, grain boundaries and point dislocations in determining material properties such as rigidity, strength, flexibility, and elasticity is well known [1]. However, in *nonequilibrium* systems the situation is more complex [2]. Nonlinear dynamical systems exhibit more complicated ''defect'' solutions such as kinks and propagating fronts [3], as well as more recent observations on spirals or targets in systems such as convection [4] or the Belusov-Zhabotinsky reaction [5]. These have been shown to play an important role in the transition of spatially ordered systems with wave dynamics to spatial decoherence and turbulence [6].

The tools for treating discontinuous perturbations are also less developed in the nonequilibrium case. Since defects demarcate the border between phases of the system, the homotopy structure of phase space at equilibrium has been used to classify the transitions between the phases [7]. This has been less effective in nonequilibrium systems, where the topological properties are not always of relevance.

What is clearly lacking is a nonequilibrium system that is rich enough to exhibit interesting ''defect'' structure and a long range influence of the discontinuous perturbation, while being simple enough to handle analytically. We present here such an example, a wetting front in which a spatial inhomogeneity is controllably inserted by changing the local permeability in a precise fashion. The advancing front is perturbed by a change in permeability, and creates an angle difference at the border between areas with different permeability coefficients.

We have previously shown that an undisturbed front, known to be hydrodynamically stable [8–10] exhibits very weak roughness [11]. If the paper is isotropic then the height-height correlation function $C(L)$ is predicted to be logarithmic in the spatial dimension L. The correlations can be enhanced by going to anisotropic paper with an average directional order in the fiber orientation. We have measured in that case power law correlations $C(L)\sim L^{0.4}$. Thus a front without defects is simple, stable, has very little or no correlated structure in it, and may be completely understood analytically [11]. Although the theory is fully consistent with the experimental results, an undetectable (logarithmic) scaling, does not allow a quantitative verification. One solution is to perturb the system and produce a pronounced response, without leaving the scope of the model. This is what the defects do. This approach can serve as a test to any theory that would claim to deal with strong disorder in porous media.

We are considering here the case of complete wetting. Defects in the case of partial wetting were considered previously by [12]. In that case the equilibrium energy considerations and balance of forces dictate a completely different configuration and steady state profile than the one we observe. Defects have also been considered in the context of front propagation for the restricted solid on solid (RSOS) model and the equivalent Kardar-Parisi-Zhang (KPZ) equation [13]. No experimental verification of any of these predictions has been reported.

In this paper we treat the conceptually simple problem of a wetting front propagating in a porous medium with two different permeabilities. The boundary between them is a discontinuous perturbation. In Sec. II we develop the theoretical approach that accounts for the influence of the discontinuous perturbation on the front. We first present the equations of motion, then show that steady state solutions exist only for a change in *porosity* but not in *capillarity*. We show why a naive perturbative approach does not work, and then proceed to present a more complete theory for the two dimensional flow field, based on assumptions of side flow (that we verified experimentally) in a region adjacent to the front. In Sec. III we describe the experimental and conceptual setup—including a simple technique of depositing printing toner with a laser printer as a controlled method for producing defects in the medium. We find that the theoretical assumptions agree with the experimental conditions. In Sec. IV

we compare the predictions of the theory regarding the ''defect'' structure with the experimentally measured profile in a quantitative fashion, yielding very satisfactory agreement. Section V includes some conclusions, perspectives, and thoughts for the future.

II. THEORETICAL ANALYSIS OF THE PROBLEM

The motion of fronts in a porous medium was extensively studied in the context of two immiscible fluids [8]. The basic physics of these phenomena is that of two dimensional flow of water in the wet domain of porous media bounded by the moving front and the walls. The driving mechanism of the moving front is the capillarity, which creates a pressure jump P_0 at the air-water boundary. The propagation rate in a medium that is characterized by a spatially fluctuating local permeability $\kappa(\vec{r})$, obeys Darcy's law:

$$\vec{v} = -\kappa(\vec{r})\vec{\nabla}P(\vec{r},t), \tag{2.1}$$

where $P(\vec{r},t)$ is the site dependent pressure. The equations of continuity for the velocity give the following equations for the pressure:

$$\nabla[\kappa(\vec{r})\vec{\nabla}P(\vec{r},t)] = \vec{0}. \tag{2.2}$$

If the parameter κ is uniform then the equation of motion for the pressure will simply be the Laplace equation.

The boundary conditions for a flow that is driven by constant capillary forces are as follows: (1) A capillary pressure $-P_0(r)$ along the moving boundary. (2) Zero pressure on the back end of the sample that is immersed in a fluid reservoir. (3) Zero normal flow on both sides of the sample. The interface velocity v_n is given by

$$v_n = -\hat{n}\cdot\kappa(\vec{r})\vec{\nabla}P(\vec{r},t), \tag{2.3}$$

where $\hat{n}$ is the normal to the interface.

In the simplest case where there is no variation of κ and P_0 and it is well known that the solution is a flat front propagating at

$$v_n = \frac{\kappa P_0}{h} \tag{2.4}$$

and the front slows down during its propagation [14]:

$$h^2 = \kappa P_0 t. \tag{2.5}$$

A. Definition of the discontinuous perturbations and steady state solutions (SSS)

We are interested in the case where there are variations in the parameters of the medium. The outstanding question is how will the flat line of a noiseless system be modified when there are changes in the system parameters. In particular we try to deal with a defect. It is defined in an infinitely long channel of width L, with y the direction of propagation and x the orthogonal coordinate. We are interested in a paper with two values for $\kappa(\vec{r})$ and/or $P_0(\vec{r})$ (see Fig. 1)

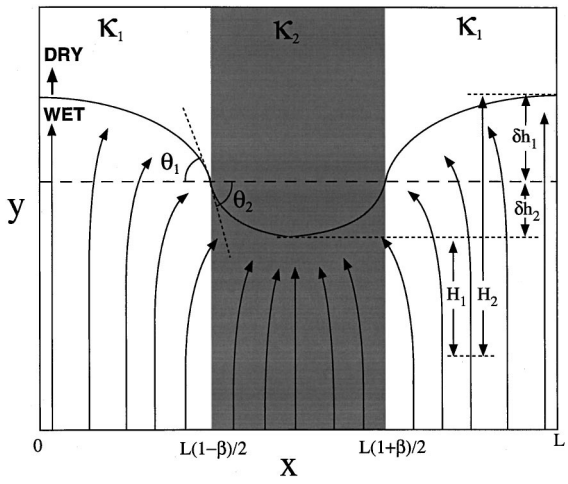

FIG. 1. A representation of the form of a steady state solution, as the front propagates from the wet to the dry region, in the combined regions of κ_1 and κ_2. The arrows schematically mark the flow lines. $\delta h_{1,2}$ represent the relative width of the first and second regions. The angles $\theta_{1,2}$ are the angles near the defect.

$$P(x),\kappa(x) = \begin{cases} P_1,\kappa_1, & 0<x<L(1-\beta)/2 \\ P_2,\kappa_2, & L(1-\beta)/2<x<L(1+\beta)/2 \\ P_1,\kappa_1, & L(1+\beta)/2<x<L, \end{cases} \tag{2.6}$$

where β is the fraction of the system size that has the permeability κ_2, and the indices 1, 2 stand for the two domains. The velocity under the same potential gradient will be different in the two media so that there is side flow, taking fluid from the slow region to the fast one. One could expect two possible scenarios for the interface shape after a long time. The first possibility is the existence of a SSS of the form

$$h(x,t) = \overline{h}(x) + H(t), \tag{2.7}$$

where $H(t)$ is a uniform displacement of the front with time, which is much larger than the time independent $\overline{h}(x)$. The second possibility is unbounded growth of the profile resulting in a scaling solution with the shape

$$h(x,t) = f(x)t^{1/2}. \tag{2.8}$$

These two possible scenarios are realized by the two different changes in the medium properties that a discontinuous perturbation can make—changes in porosity versus changes in capillarity.

In the case of changes in capillarity P_0 there will be two different driving capillary forces, P_1 and P_2, in the two domains. We will show that this corresponds to the case of a scaling solution. Suppose that the interface has a finite width δh and that the lower part has passed a distance $h_1 \gg \delta h$. The gradient in pressure in the fast domain is related to P_1, since it is a boundary condition for the Laplace equation on the fast side (the question of how close it is and what is the exact gradient will depend on β and on the exact solution). However, the characteristic pressure gradient is $(P_2-P_1)/\delta h$ so the characteristic velocity will be $v \sim \dot{\delta h} = \kappa(P_2-P_1)/\delta h$. On the other hand the propagation rate in the slow region is $v \sim \dot{h}_1 = \kappa P_1/h_1$. Suppose that there was some solution in

which δh becomes fixed. For a large enough h_1 the velocity $\dot{\delta h}$ will be much larger then $\dot{h}_1$. Using these velocities one can write decoupled equations for h_1 and δh with solutions similar to Eq. (2.5) so the ratio between them can be estimated to be

$$\frac{\delta h}{h_1} \sim \left(\frac{P_2 - P_1}{P_1} \right)^{1/2}. \tag{2.9}$$

This indicates that there is a scaling solution of the type given in Eq. (2.8) and not a SSS. This type of solutions will not be discussed in this paper.

On the other hand, the case of changes in porosity $\kappa_1 \neq \kappa_2$ the situation is quite different. Gradients will be bounded, so in this case we expect to see a steady state solution of the type of Eq. (2.7). The actual shape will depend on the parameters $\beta, \kappa_1, \kappa_2$. In Fig. 1 we show the basic shape of such a solution.

Since we shall find that the experimentally observed profiles follow this form we focus on SSS surface profiles in the limit of long times. This is analytically a hard problem because of the nonlocality of the potential. We will first derive some general laws for those profiles and then try to calculate them using various methods.

B. The steady state solution and its general properties

We now go on to derive implicit equations for the SSS front position. The front propagates in the y direction at a velocity V_s that is different from the velocity of fluid v_y. For any front position $h(x)$ the demand for a SSS is a uniform velocity V_s of the front. Geometrically, the fluid velocity normal to the front will translate to a front velocity by

$$V_s = \frac{v_n^h}{\cos[\theta^h(x)]}, \tag{2.10}$$

where v_n^h is the front velocity calculated using Eq. (2.3) from the height-dependent pressure, $\theta^h(x)$ is the angle between the x direction and the front at the position x and $\cos[\theta^h(x)] = (dh/dx)/\sqrt{1+(dh/dx)^2}$. We want to find a unique $h(x)$ for which the solution for the pressure generates a uniform surface velocity. This is a nonlocal and nonlinear problem.

The following discussion considers some of the general properties of the SSS. We first discuss the basic scaling properties of the solution $\bar{h}(x)$. The equations of motion are invariant under the transformation $x \to x/L$, $y \to y/L$, and $\bar{h} \to \bar{h}/L$. This indicates that the solution $\bar{h}(x)$ has the scaling form

$$\bar{h}(x) = L f(x/L), \tag{2.11}$$

where f is an unknown scaling function and the width of the solution scales as L. In what follows we shall always rescale the system width to $L=1$.

In addition one can transform $\kappa_i \to \lambda \kappa_i$. Thus the SSS shape depends only on κ_1/κ_2. The relevant parameter that defines the solution is the contrast:

$$\delta\kappa = \frac{\kappa_2 - \kappa_1}{\kappa_1}. \tag{2.12}$$

These two relations create a possibility to make real predictions about real experimental problems, since otherwise it would be hard to estimate and relate size and contrast in those systems to a theoretical model. This point will be addressed further in the part dealing with comparison of experiment and theory.

We next discuss a law that relates the angles θ_1 and θ_2 (see Fig. 1). Consider the pressure near the surface and the defect. Since the front velocity there is a constant V_s, the velocity of the interface in the y direction is $V_s \cos^2(\theta_i)$. Thus the gradient of the potential in the y direction is $V_s \cos^2(\theta_i)/\kappa_i$. Since the potentials should be equal in the two domains along the discontinous perturbation we get

$$\frac{\cos^2(\theta_1)}{\kappa_1} = \frac{\cos^2(\theta_2)}{\kappa_2}. \tag{2.13}$$

This is analogous to Snell's law in optics: $\sin(\theta_1)/\kappa_1 = \sin(\theta_2)/\kappa_2$. However, it has very different consequences. If $\kappa_1/\kappa_2 \sim 1$ the equation is valid for any two close angles. However, if $\kappa_1/\kappa_2 \gg 1$ then $\theta_2 \to \pi/2$ [$\theta_1 = 0$ gives $\cos^2(\theta_2) = \sqrt{(\kappa_1/\kappa_2)}$]. This is an indication of the asymmetry between the slow and fast regions of high contrasts.

We go on to discuss the velocity V_s of the SSS front. The average pressure gradient in the y direction is $P_0/[H + h(x)]$ where H is, as stated before, much larger then $h(x)$. So the average propagation rate is $V(x) = \kappa(x)\nabla_y P(x,y) = \kappa(x) P_0/[H + h(x)]$. Since κ has two values in the two domains we get two different average velocities: $v_i = \kappa_i P_0/H$. However, V_s is constant. The obvious conclusion is that the flow over most of the channel is with the two former characteristic velocities while in a small region near the SSS front the two flows are combined by side flow to create a common propagation rate in the channel. Because of conservation of current the SSS propagation rate should be

$$V_s = \frac{P_0[\kappa_1\beta + \kappa_2(1-\beta)]}{H} = \frac{P_0\bar{\kappa}}{H}, \tag{2.14}$$

where $\bar{\kappa}$ is the weighted average of κ in the system.

This in fact, gives us information about the side flow. Assume that $\kappa_2 \geqslant \kappa_1$. Since the propagation rate in the fast region is larger than the average, an amount proportional to the deficit in the current should be transported to the slow region. Therefore the total lateral current I_x in the fast domain (κ_2) should be

$$I_x = (V_2 - V_s)(x - 0.5) \tag{2.15}$$

and in the slow region (κ_1) it will be

$$I_x = (V_s - V_1)x. \tag{2.16}$$

Any solution must satisfy these equations.

C. An approximate analysis for the steady state form for all contrasts

We now turn to calculate the shape of the SSS. We note that it is defined as $h=\overline{h}(x)+H(t)$. The length $H(t)$ will scale according to the average propagation rate, while $\overline{h}(x)$ is time independent. Since we know that the front is flat at zero contrast it is natural to first try a perturbation theory with the strength of the contrast as a parameter. From this approach one can derive a first order estimate for the profile. In general, this should be a useful approach.

However, we find that in our case this perturbation theory is a problematic method. The sharp change in the parameters of the problem leads to divergences in the second order theory that do not appear in the original problem, and to a first order solution that is not smooth enough. So while the failure of this approach is an interesting issue, the details of this approach are given in the Appendix.

In lieu of a perturbation approach, we turn to an approximate theory, which will nevertheless be good to all orders. We first remind the reader of our results on the steady state propagation rate [Eq. (2.14)]. We found out that the velocities in the two regions are different over most of the system and that there is a small region near the front where there is side flow and modifications in the gradients [17]. We denote the distances of this transition point from the points of zero slope of the interface in the two regimes as H_1 and H_2 and define the pressure at this point as $\overline{P}$. The average gradients in the active region will be

$$\langle \nabla_y P(x,y)\rangle = \frac{P_0-\overline{P}}{\overline{h}(x)}, \tag{2.17}$$

where $\overline{h}(x)$ is the distance from the line defined by H_1, and is a refinement of the definition in Eq. (2.7). If we assume that this gradient is constant then the average pressure gradient in the x direction can be estimated to be $\nabla_x\langle P(x,y)\rangle = k_i[\nabla_x\overline{h}(x)(P_0-\overline{P})/\overline{h}^2(x)]y$. From this we can find the current in the x direction:

$$I_x=-\int_0^{\overline{h}(x)} k_i \frac{\nabla_x\overline{h}(x)(P_0-\overline{P})}{\overline{h}^2(x)}\, z\,dz = -\kappa_i\nabla_x\overline{h}(x)\,\frac{P_0-\overline{P}}{2}. \tag{2.18}$$

This equation together with the equations for the side flow, (2.15) and (2.16), allow a calculation of the shape of the interface. The differential equations for $\overline{h}(x)$ in the two domains are

$$\kappa_2\nabla_x\overline{h}(x)\,\frac{P_0-\overline{P}}{2} = -(V_2-V_s)(x-0.5), \tag{2.19}$$

$$\kappa_1\nabla_x\overline{h}(x)\,\frac{P_0-\overline{P}}{2} = -(V_1-V_s)x. \tag{2.20}$$

The solutions for these equations are parabolas with curvatures E_1 and E_2:

$$h_1(x)=H_1+\frac{(V_s-V_1)}{\kappa_1(P_0-\overline{P})}\,x^2=H_1-E_1x^2, \tag{2.21}$$

$$h_2(x)=H_2+\frac{(V_s-V_2)}{\kappa_2(P_0-\overline{P})}\,x^2=H_2+E_2(x-0.5)^2. \tag{2.22}$$

It is easy to find that

$$E_2=E_1\,\frac{\kappa_1\beta}{\kappa_2(1-\beta)}. \tag{2.23}$$

Estimating the potential gradients in the two extrema by the scale H_1 we get $P_0-\overline{P}=P_0\overline{\kappa}H_1/\kappa_1 H$. Since H_1 is related to H_2 as $\kappa_1/H_1=\kappa_2/H_2$ we find

$$H_2-H_1=\frac{\kappa_2}{\overline{\kappa}H_1}\left[\frac{\beta^2}{4\kappa_1}(\overline{\kappa}-\kappa_1)+\frac{(1-\beta)^2}{4\kappa_2}(\kappa_2-\overline{\kappa})\right]. \tag{2.24}$$

Since $H_2-H_1=H_1(\kappa_2/\kappa_1-1)$ we can finally get

$$H_1^2=\frac{\kappa_1\kappa_2}{\overline{\kappa}(\kappa_2-\kappa_1)}\left[\frac{\beta^2}{4\kappa_1}(\overline{\kappa}-\kappa_1)+\frac{(1-\beta)^2}{4\kappa_2}(\kappa_2-\overline{\kappa})\right]. \tag{2.25}$$

Note that H_1 *does not depend* on the total length H. This confirms our original expectation. It also enables us to calculate the following angles:

$$\tan(\theta_1)=2\,\frac{(\overline{\kappa}-k_1)}{\overline{\kappa}H_1}\,x, \tag{2.26}$$

$$\tan(\theta_2)=2\,\frac{(\overline{\kappa}-k_2)\kappa_1}{\overline{\kappa}\kappa_2H_1}\,(x-0.5). \tag{2.27}$$

From the angles one can calculate the heights of the parabolas in both regions, which we denote as δh_1 and δh_2. These two parameters turn out to be the convenient variables for comparison with the experiment.

It is interesting to discuss the two limits $\delta\kappa\ll 1$ and $\delta\kappa\gg 1$. One can easily find that when $\delta\kappa$ is close to 0,

$$H_1=\frac{\sqrt{\beta(1-\beta)}}{2}, \tag{2.28}$$

$$\tan(\theta_1)=\tan(\theta_2)=\delta\kappa\sqrt{\beta(1-\beta)}, \tag{2.29}$$

$$\delta h_1=\delta\kappa\,\frac{\sqrt{(1-\beta)\beta^3}}{4}, \tag{2.30}$$

$$\delta h_2=\delta\kappa\,\frac{\sqrt{(1-\beta)^3\beta}}{4}, \tag{2.31}$$

while for large $\delta\kappa$,

$$H_1=\left(\frac{\kappa_1}{(1-\beta)\kappa_2}\right)^{1/2}, \tag{2.32}$$

$$\tan(\theta_1)=\beta(1-\beta)\,\delta\kappa^{-1/2}, \tag{2.33}$$

$$\tan(\theta_2)=\left(\frac{\delta\kappa}{\beta(1-\beta)}\right)^{1/2}, \tag{2.34}$$

$$\delta h_1 = \frac{\sqrt{\delta\kappa(1-\beta)^3\beta}}{4}, \tag{2.35}$$

$$\delta h_2 = \delta\kappa^{-1/2}(1-\beta)^{5/2}. \tag{2.36}$$

In the regime of $\delta\kappa \ll 1$ a linear dependence on $\delta\kappa$ is observed, as one gets from the simple perturbation theory. However, when the contrast is large we observe a change to a dependence on $\delta\kappa^{0.5}$. Then the angles and the width in the fast region decay as $\delta\kappa^{-0.5}$ while in the slow region the width growth as $\delta\kappa^{0.5}$ and the angle θ is closer to 90°. The crossover is expected at $\delta\kappa \sim 1$.

To summarize, the main results of the theory are as follows:

(a) The interfaces are parabolic [Eq. (2.22)].

(b) The height of the region in which sideflow occurs, H_1, is given in terms of the permeabilities and the defect width β.

(c) The parameters of the parabolas can be calculated once H_1 is known, for example, the angles at the edges are given by Eq. (2.27).

(d) We find that there are two basic scaling regions, as a function of the contrast $\delta\kappa$. For example, the scaling of $\delta h_{1,2}$ changes drastically in the two limits. In the low $\delta\kappa$ region both heights are linear with $\delta\kappa$. In the high $\delta\kappa$ regime δh_1 increases as a square root while δh_2 decreases as a square root [Eqs. (2.32)].

Our results are only approximate mainly due to the transition from Eq. (2.17) to Eq. (2.18), which is based on the assumption of a constant gradient in the y direction. We can check our estimates against the exact cosine relation (2.13) derived previously and against the perturbation theory.

It is easy to see that the constant cosine relation is kept in the nonlinear domain since $\theta_2 \sim \pi - \delta\kappa^{-0.5}$ and $\theta_1 \sim \delta\kappa^{-0.5}$. However thereis a mismatch in the value (the cosine relation is not 1 but some other constant related to β). The mismatch is small as long as β is not too close to zero or one.

In fact one can use the cosine relation (2.13) as a consistency check for the parabolic solution. We use it to find another relation between E_1 and E_2. We first note that

$$\tan(\theta_1) = E_1\beta, \tag{2.37}$$

$$\tan(\theta_2) = E_2(1-\beta). \tag{2.38}$$

Using this we can write the cosine relation using the E_i's.

$$\kappa_1(1+\beta^2E_1^2) = \kappa_2[1+(1-\beta)^2E_2^2]. \tag{2.39}$$

Using this relation and using Eq. (2.23) we find that E_1 is

$$E_1^2 = \frac{\kappa_1}{\kappa_2\beta^2}. \tag{2.40}$$

So the approximate method may also be inaccurate in the small $\delta\kappa$ limit, since we get an interface even for zero contrast ($\delta\kappa = 0$).

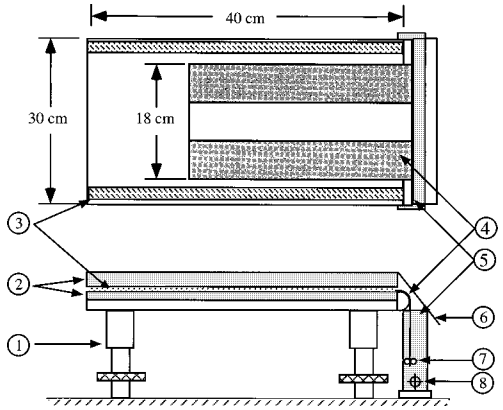

FIG. 2. Schematic representation of the setup. Top view (top) and side view (bottom). (1) Adjustable supports, (2) glass top and bottom, (3) metal spacers, (4) filter paper with defects, (5) immersion cell, (6) plastic cover to prevent evaporation, (7) metal weights, (8) filling and emptying holes.

III. THE EXPERIMENT

A. Apparatus

The setup is shown schematically in Fig. 2 (see also Ref. [11]). The experiment consists of a capillary driven wetting front of clean (deionized) water, propagating horizontally in filter paper. The paper medium (filter paper made by Whatman, grade 91), of horizontal dimensions 20×30 cm^2 (4 in Fig. 2), is sandwiched between glass top and bottom plates of dimensions 40×30 cm^2 (2 in Fig. 2). The top glass plate is thick (1.2 cm) to minimize stress bending, which may affect the front. The top plate rests on two thin metal spacers (3 in Fig. 2), of thickness 0.018 cm. The spacers are slightly thinner than the paper (paper thickness: 0.02 cm). Consequently the paper touches both top and bottom plates. One end of the paper protrudes from the plates and is immersed in a rectangular cell, of dimensions $32 \times 8 \times 2$ cm^3 (5 in Fig. 2). The cell is filled from below to minimize fluctuations in the initial conditions (8 in Fig. 2). Metal weights are attached to the bottom of the immersed side of the paper to improve the uniformity of the initial wetting (7 in Fig. 2). Evaporation is prevented by the glass top and a plastic cover near the immersed edge (6 in Fig. 2).

A salient property of wetting fronts in porous media is their slowing down [14]. We define the proportionality constant $\alpha = \kappa P_0$ by Eq. (2.5) (see inset in Fig. 3):

$$\langle h \rangle^2 = \alpha t. \tag{3.1}$$

Generally α depends on the properties of the paper and of the fluid $\alpha \approx \gamma r \cos(\theta)/\eta$, where γ and η are the fluid surface tension and viscosity, respectively, r the typical pore size in the paper, and θ the wetting contact angle [14]. α is an experimental estimate of κP_0 [Eq. (2.5)].

The width of the front, defined as the distance from the completely dry region to the saturated wet region, is smaller than 0.1 cm. This allows us to get precise measurements of α. We measured $\alpha = 0.22 \pm 0.01$ cm^2/s for propagation of the untreated paper, parallel to the effective fiber orientation. Plugging into Eq. (3.1) $\gamma = 73$ erg/cm^2, $\eta = 0.01$ g/cm s, and $r = 10$ μm (the particle retention size given by the manufac-

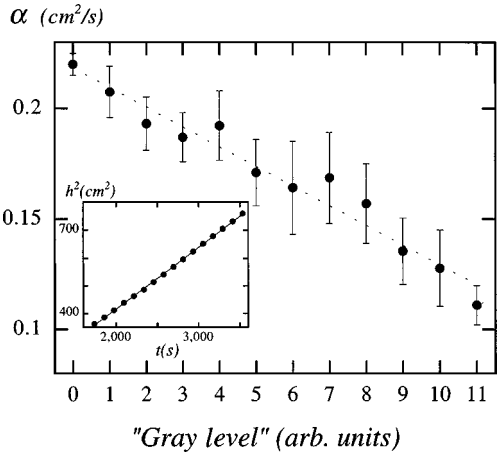

FIG. 3. The effective propagation rate α as a function of the ''defect strength'' or ''gray level'' of printing. The gray level is the amount of *toner* adsorbed on a square grid. Gray level$=0$ is plain paper. The inset shows the time dependence of the square of the interface position for the particular case of gray level$=0$. α is the slope in that graph.

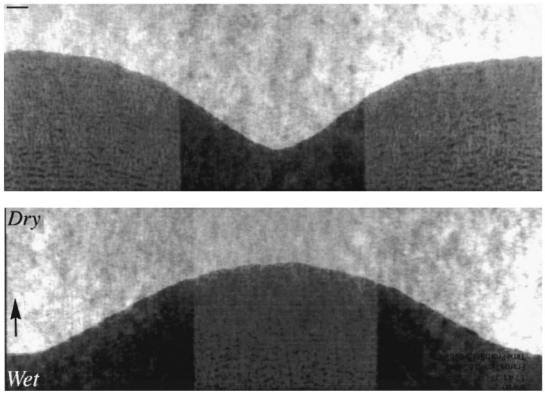

FIG. 4. A wetting front with defects. The top and bottom show the fast-slow-fast regime and slow-fast-slow configurations, respectively (the printed parts are darker). The front propagates from bottom to top. The pictures were taken about 30 min from the beginning of the run. The papers are 18 cm wide with a width distribution between the slow ($\alpha=0.11$ cm^2/s) and fast ($\alpha=0.22$ cm^2/s) zones of $\frac{1}{3}$, $\frac{1}{3}$, $\frac{1}{3}$. The scale bar is 1 cm.

turer) gives $\theta=88°$ (for similar measurements in other fluids see the third part of Ref. [14]).

A typical run duration is 1 h (see inset in Fig. 3). The paper was not pretreated: oven drying and storage in a nitrogen atmosphere (to minimize humidity and prewetting effects) did not change the average α and did not significantly affect its statistical spread.

To apply *defects* we create regions with different α. A main experimental advantage of using defects is the pronounced profile that they induce. Consequently the statistical difficulties incurred in our previous work on free wetting fronts (Ref. [11]) are considerably reduced.

In practice, there are a number of ways to treat paper and create defects. We tried mechanical treatments such as pressure, with and without high temperature, as well as other treatments such as coating with silicone and wax. None of these methods was as good as printing, in terms of uniformity and the reproducible effect on the front. There are also many fluids that can be used instead of water. Organic fluids are advantageous because they do not interact with the fibers [14]. However, the width of the front created by fluids like tetradecane and silicone oil is an order of magnitude larger than the width of the front created by water.

Our defects are produced by printing a black (or gray) stripe with a laser printer (we use an Apple Laser Writer Pro630 printer with M6018*G*/A toner). The printing slows down the propagation, presumably by partially clogging the paper and reducing the area available to the propagating fluid. The strength of the discontinous perturbation could be varied by using different shades of gray scaling (on the same grid). We consider plain paper as a defect of strength zero. The effect of the *gray level* on α, which represents our ''defect strength'' is shown in Fig. 3. α varies from 0.11 ± 0.02 cm^2/s for black paper, to 0.22 ± 0.02 cm^2/s for untreated white paper. Although printing has a macroscopic effect on the front, it is a surface treatment. Inspecting a cross section of the printed paper under a $20\times$ microscope objective, we found that about 10% of the thickness of the paper is covered by the printing toner.

The paper is placed with the printed face down. This improves the optical contrast between the wet and the dry sides of the front (we use reflected light). The imaging equipment consists of a charge-coupled device camera (Sony XC-75CE) with a 28 mm lens (Nikon 1:35), placed about 1 m above the paper sample. The digitization matrix is 736×512 and typically covers 18×12 cm^2. The geometrical distortion of the image was less than 2%. The accuracy in resolving the front is about 5 pixels. In a typical run we averaged over 20–30 frames. This was done with a code that we added to the image analysis software ''NIH Image 1.6.'' The code automatically identifies the propagating front and stores it on a disk at predetermined steps in time or space. The algorithm is based on subtracting two consecutive images and then thresholding $n\sigma$ below the average, where σ is the standard deviation of the picture gray levels and n a number that characterizes the noise in the image. This algorithm is capable of identifying a wide variety of fronts [15].

B. Characterizing the fronts

In Fig. 4 we show two typical profiles of a wetting front with defects, in the configurations fast-slow-fast ($\alpha=0.22$, 0.11, 0.22 cm^2/s, top picture in Fig. 4) and slow-fast-slow ($\alpha=0.11$, 0.22, 0.11 cm^2/s, bottom). The slower propagation in the printed region induces a curved profile, extending over the entire system. The flattening of the front towards the edges (lateral paper-air boundary) is related to the fact that there is no side flow at the edge. This justifies the use of periodic boundary conditions in the theoretical description.

In Fig. 5 we show eighteen consecutive digitized profiles in the slow-fast-slow configuration. The profiles in the picture represent the experimental raw data and include the end of the transient leading to a steady state (first 2 cm) followed by the experimental steady state regime. The small scale noise in the profiles is larger than the digitizing noise (0.1 cm). It is inherent in all the runs and must be averaged over. About 10 profiles per run suffice to smooth the profile. The noise is especially evident at the edges, often influencing the flattening mentioned above. However, the signal to noise ra-

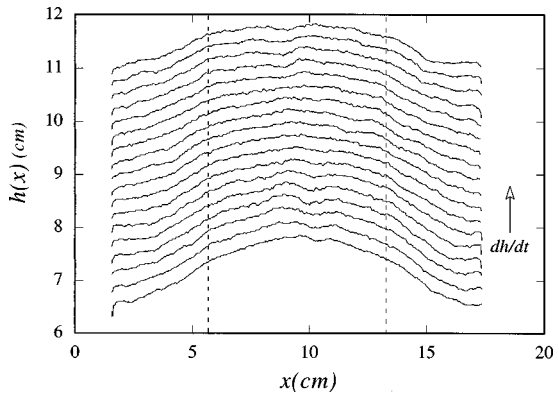

FIG. 5. A series of consecutive profiles (propagating from bottom to top) in the steady state regime. The widths distribution is $\frac{1}{4}$, $\frac{1}{2}$, $\frac{1}{4}$. The regions are marked by the dashed lines.

tio of the profile is significant even without averaging. We have previously shown that the system without defects develops a large scale bias [11]. In the present case, the profile induced by the printing prevails over the bias, which is small in comparison and does not interfere with the measurement.

IV. QUANTITATIVE COMPARISON BETWEEN THEORY AND EXPERIMENT

Our theoretical approach was centered on the fact that the flow field is fully two dimensional. The importance of this was seen in the case of roughening [11], where two dimensionality introduces a nonlocal term in the equation for the front. This also serves to rule out a description in terms of KPZ-like models [16]. The steady state front and $\langle\alpha\rangle$ are obviously sustained due to *side flow* from the fast to the slow regions. To identify this flow experimentally, we resorted to a dye visualization technique. A few ink drops are spread on the paper in anticipation of the front. The ink is swept by the flow, leaving behind a track of the flow trajectory. This is shown in Fig. 6, where a horizontal array of 15 drops of black ink was placed in the way of the front. Notice that the polydisperse ink colloids separate according to their size

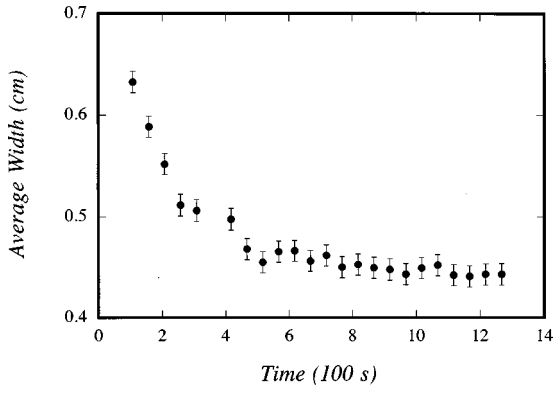

FIG. 6. An array of black ink spots is placed in front of the interface. The thin line serves as a guide to show the interface after the experiment was stopped. The swept ink marks the flow lines. The side flow from fast to slow regions is evident (see text). The run was stopped after the front reached the position shown in the figure and the paper was put to dry. The faint lines above the front represent weak wrinkling which is due to the drying process.

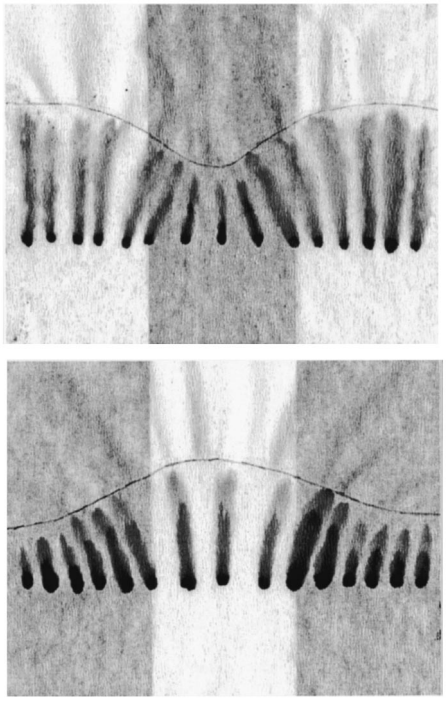

FIG. 7. The average width of the profile as a function of time show that the system attain a steady state. The run in the picture is slow-fast-slow of width 18 cm. In this run $\alpha = 0.22 \pm 0.01$ cm^2/s.

(and color) as in chromatography [18]. As expected from a flow system, the flow lines, which mark the corresponding interface propagation rate, are perpendicular to the front.

The two basic features of the model that enable us to derive theoretical predictions are that the height scales with the system size and that the shape depends only on the contrast $\delta\kappa = (\kappa_2 - \kappa_1)/\kappa_1$. We could not check the system size dependence experimentally, since for small system size the noise was comparable to the defect profile. Even so, we can rely on them to compare theoretical and experimental results using the α values.

An important ingredient in our model is the existence of a SSS as shown in Fig. 5. Our theory predicts that a SSS exists only if the printing changes the volume available to the fluid, but leaves the capillary forces unchanged. This supports the idea that the toner acts mainly to clog the paper and change the permeability. The process of approaching a steady state can be described by the width of the profile, which decreases to a constant value. Figure 7 shows the average width of the profile as a function of time from the beginning of the run. The steady state is attained after an initial transient lasting about one width of the largest stripe in the paper ($L/2$). We use this as a criterion for attaining a steady state and analyze the profiles in that regime.

The existence of a steady moving profile dictates a global average propagation rate, given by Eq. (2.14), for the hybrid system. The propagation rate is defined by the average over the individual α's, weighted according to the relative widths of the stripes. This result is shown in Fig. 8. The figure was obtained by repeating the experiments with different relative widths β. A linear regression is done on the experimental data, and the fitted line is shown in the plot. The fact that the data appear to fall on a straight line is consistent with the

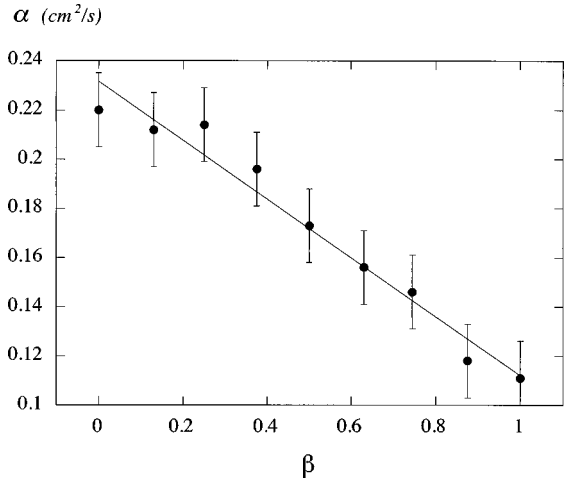

FIG. 8. α as a function of the relative printed portion: $\beta = L_{\text{printed}}/L_{\text{total}}$. The experiments were performed in a slow-fast configuration of varying relative width. Zero in the graph refers to plain paper and 1 to printed paper. Each point is the average of three measurements. The typical statistical spread is represented by the error bars. We estimate a line by a linear fit to the points. The graph is linear in accord with Eq. (2.14).

theoretical prediction of Eq. (2.14).

The theory gives an explicit prediction for the shape of the profile. This is a parabolic curve whose two parameters are defined by the width L and by the permeability contrast $\delta\kappa$. The comparison of the measured profiles to the theoretical prediction of a parabolic shape yields good results (Fig. 9). The fit is carried out separately for the fast and for the slow region, and is good in both domains. The quality of the fit is maintained throughout the width of the domains. The fitting parameters compare well to the theoretical predictions, and are described below. At the defect, the theory matches the interface from both domains, while the derivative is discontinuous there. In practice, the profile is smoothed out by the flow and the derivatives are continuous.

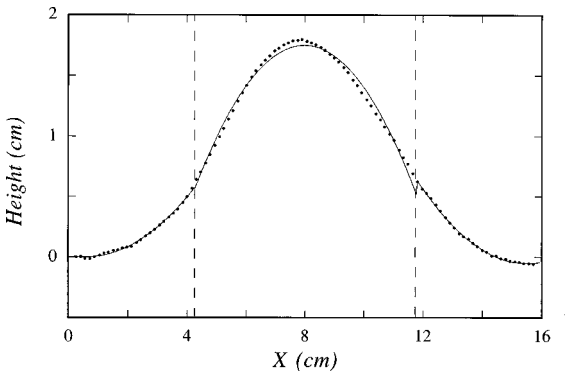

FIG. 9. A comparison of the measured profiles (100 of the measured 750 points are shown) to the theoretical prediction of a parabolic shape (continuous line), as predicted by Eq. (2.22). The experimental curve is an average over 10 fast-slow-fast profiles for $\lambda = 0.41$. The boundaries are marked by the vertical dashed lines. The continous lines are the best fit to a parabola $y = ax^2$. The parameter a is -0.09 ± 0.01 cm^{-1} and -0.04 ± 0.01 cm^{-1} for the slow and fast regions, respectively. In the fast region we averaged over the two sides. The fits display a discontinuity in the derivative. In the experiment the discontinuity is smoothed out due to the flow. As seen in Fig. 9, this gives a slight deviation at the discontinous perturbation, and a corresponding jump in the fitted parabolas.

A delicate point, emphasized by the theory, regards the symmetry between the profiles in the fast-slow-fast and the slow-fast-slow configurations. In principle, the two configurations should be symmetric to translations by half a ''wavelength,'' i.e., by one stripe. Conceptually, this is implied by the periodic boundary conditions assumed in the theory, and is experimentally equivalent to an infinite number of stripes. This is most closely approached in the $\frac{1}{4}, \frac{1}{2}\frac{1}{4}$ configuration, and is supported by the flattening of the interface near the paper-air boundary.

Furthermore, the theory predicts that for small contrast the profile in the fast and in the slow domains should be symmetric under an up-down inversion with respect to the flow direction. This symmetry should be lifted by a rise in the contrast. This can be checked by comparing a slow-fast-slow profile with an inverted profile of the fast-slow-fast stripe formation as a function of $\delta\kappa$. In Fig. 10 we vary the discontinous perturbation strength from $\delta\kappa = 0.1$ to $\delta\kappa = 0.99$. We obtain symmetric fronts for small defect strength ($\delta\kappa < 0.15$), which is gradually lost as the defect strength is raised above $\delta\kappa = 0.5$. The discontinuity of the derivatives described in the paragraph above exists only for defects with asymmetric profiles.

We can use H_1 to get $\theta_{1,2}$ [Eq. (2.27)]. Knowing the derivatives at the edges of the parabola and its width, we can obtain the parameters $E_{1,2}$ and also the heights $\delta h_{1,2}$. This prediction is given in the inset of Fig. 11. This presents a stringent test of the agreement between experiment and theory, since there are no adjustable parameters for the fit. In the main part of Fig. 11 we show the remarkable agreement (taking the experimental difficulties into account) between experiment and prediction. The data are normalized by the size of the system L. The experimental regime is right at the point of transition predicted by theory ($\delta\kappa \approx 1$), and shows the separation of the two lengths δh_1 and δh_2, but does not reach into the change of slope predicted for δh_2. The points in the figure are derived only from the central portion of curves in Fig. 10 (''fast'' from slow-fast-slow and ''slow'' from fast-slow-fast). This selection minimizes the effect of the water-air interface on the paper boundaries.

The existence of a characteristic length H_1 from the front, above which side flow occurs and below which the flow is uniformly forward, is an essential tenet of the theory. To check its existence we turned again to ink tracers, placing them this time both in front and behind the front. Figure 12 depicts the transition to side flow as a function of distance from the front. The dye was placed when the front was at the second spot from the left. We then let the front propagate until close to the next ink spot. Looking behind the front, we clearly see a point at which there is no longer any side flow. H_1 is very hard to determine precisely with this experimental technique, but we estimate it as $H_1 \approx 0.44$ (about 7 cm divided by the width of the paper 16 cm). The theoretical value [given by Eq. (2.25)] $H_1 = 0.7 \pm 0.05$.

V. CONCLUSIONS

In summary, we have presented a detailed study, experimental and theoretical, of a nonequilibrium flow system with

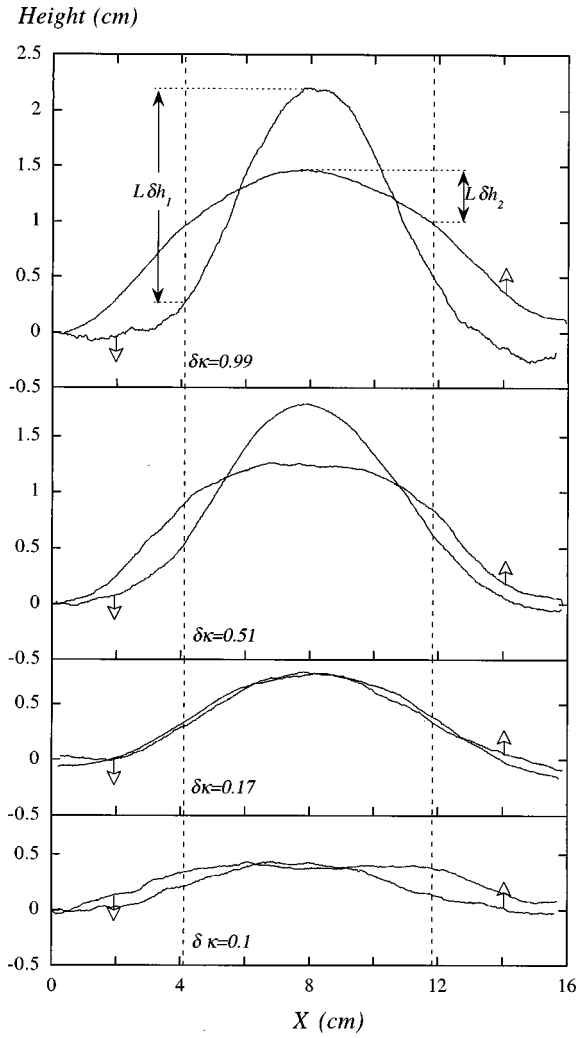

FIG. 10. The average profiles for $\delta\kappa=0.1$ (bottom), $\delta\kappa=0.17$, $\delta\kappa=0.51$, and $\delta\kappa=0.99$ (top). The graph was created by inverting the fast-slow-fast profiles and substituting zero for the left system boundary. The fast-slow-fast configuration is lower than the slow-fast-slow for $\delta\kappa=0.51$ and 0.99. For $\delta\kappa=0.1$ the defects are weak and large-scale fluctuations prevail [11]. For $\delta\kappa=0.17$ the two curves coincide. The asymmetry starts to develop for $\delta\kappa=0.51$. It grows further for $\delta\kappa=0.99$.

a propagating front, where a defect is introduced in a simple and tractable way. The theory for such flow in porous media gives predictions for profiles and velocities at different defect structures and strength. On the other hand we have an experimental system in which profiles can be controlled and precisely measured.

The first essential ingredient allowing theory and experiments to interact is the existence of steady state solutions. A change in the capillary forces (not porosity) can generate a completely different scaling solution for this problem. The comparison of theory to experiment indicates that there is no change in the capillary pressures, but we have no independent verification of this. The other essential ingredients are that the system is dimensionless, basically because $h\sim L$ and that all results depend only on the contrast $\delta\kappa=(\kappa_2-\kappa_1)/\kappa_1$. Problems of roughness and noise are avoided by having the strong perturbation of a defect, by averaging and by discussing only the steady state solution.

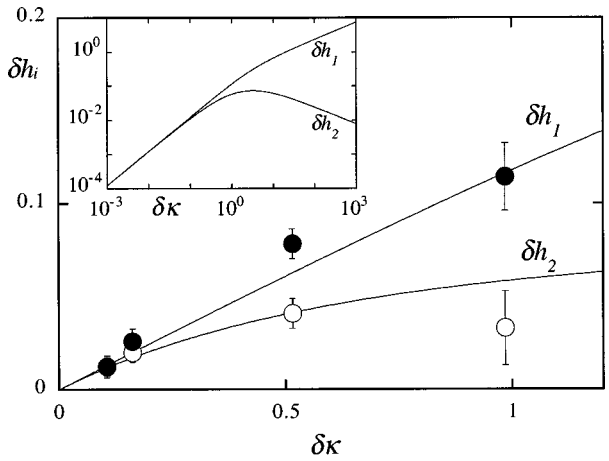

FIG. 11. The experimental and theoretical values for δh_1 and δh_2 (see text for details). The inset shows a log-log plot of the full predicted behavior. The experimental points were measured from the data presented in Fig. 10 (for both fast-slow-fast and slow-fast-slow configurations). They depict the crossover region, marked by the rectangle in the inset.

We end up with an excellent correspondence of experiment and theory, and must emphasize that there are *no free fit parameters*. In this way we obtained quantitative results for the propagation rate of the front, profile shapes and heights, the depth of the perturbed flow field and the transition to asymmetric profiles with the change of contrast.

An interesting conclusion from our work is that a local effect (defect) will have a nonlocal effect on the scale of the full system size. This is related to side flow whose existence is verified experimentally. A second remark is that the system ends up with profiles that are extremely basic: simple quadratic functions. Finally, we note the outstanding result, apparent in the perturbation theory and corroborated by the experiment, that the asymmetry between the slow and fast profiles of the steady state solution is a tendency which develops with the contrast.

The theory further predicts a transition in the scaling of profile heights from low contrasts to high contrasts occurring at $\delta\kappa\sim 1$. The range of contrast available to us in the experiment was only for $\delta\kappa\leqslant 1$ so we could observe the beginning of the transition to a different scaling but we cannot observe

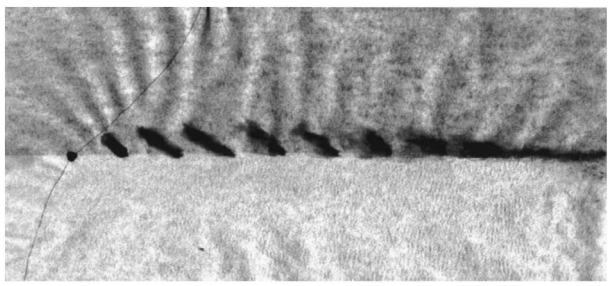

FIG. 12. A picture of a $\frac{1}{2}$, $\frac{1}{2}$ experiment in which a longitudinal array of ink drops was placed after 50 min of run (when the intersection of the front and the centerline of the paper was at the second ink drop from the left). The final position of the front is marked at the leftmost ink drop. The figure shows the transition to side flow as a function of h. Side flow only occurs up to a certain length $\overline{H}_1$.

the second scaling regime. This would be a very interesting future objective.

Theoretically, the obvious extension of this system is to vary the capillary pressures P_1 and P_2 to generate a scaling solution for the profile. This presents an interesting experimental challenge. Other extensions include random arrays of defects and the interaction between them, and introduction of fluctuations in capillary forces which will hopefully lead to complex yet tractable propagating front solutions.

ACKNOWLEDGMENTS

We take pleasure in thanking D. Mukamel for introducing us to the topic of defects. We also thank S. Alexander, O. Gat, D. Danino, A. Marmur, S. Sandow, V. Steinberg, and I. Webman for numerous helpful discussions. The work was funded in part by the Minerva Center for Nonlinear Science.

APPENDIX: CALCULATION OF THE SHAPE OF THE PROPAGATING FRONT USING PERTURBATION THEORY

Consider a front with a small perturbation in $h(x)$ and a small variation in $\kappa(x)$. The dynamics of the propagating front is given by Darcy's law:

$$\dot{h}(x,t) = -\kappa(x) P_y(h), \tag{A1}$$

where we assume $\sqrt{1+(dh/dx)^2} \sim 1$, and $\dot{h}$ is the front's propagation rate. We wish to find the SSS front propagation rate and shape in this case. We remind the reader that $\dot{h}(x,t) = \text{const}$ in this case.

To do this we expand $P(h)$ and h near an h_0 [which is some large $H(t)$ in Eq. (2.7)] in powers of a small parameter λ:

$$h = h_0 + \lambda \overline{h_1} + \lambda^2 \overline{h_2} + \cdots \begin{cases} P(h) = \phi_0(h) + \lambda \phi_1(h) + \lambda^2 \phi_2(h) + \cdots \\ \phi_i(h) = \phi_i(h_0) + \phi_{i,y}(h_0)(\lambda \overline{h_1} + \lambda^2 \overline{h_2}) \\ \quad + \frac{1}{2} \phi_{i,yy}(h_0)(\lambda \overline{h_1} + \lambda^2 \overline{h_2}) + \cdots . \end{cases} \tag{A2}$$

We also expand $\kappa(x)$:

$$\kappa(x) = \overline{\kappa} + \lambda k(x), \tag{A3}$$

where $\overline{\kappa}$ is defined in Eq. (2.14) and $k(x)$ is a normalized function that describes the geometry of the media. Insertion of these terms into the equations for the dynamics (2.2) gives up to λ^2:

$$\nabla^2 \phi_0 = 0, \tag{A4}$$

$$\vec{\nabla} k(x) \cdot \vec{\nabla} \phi_0 + \nabla^2 \phi_1 = 0 \Rightarrow \nabla^2 \phi_1 = 0, \tag{A5}$$

$$\nabla^2 \phi_2 + \vec{\nabla} k(x) \cdot \vec{\nabla} \phi_1 = 0 \Rightarrow \nabla^2 \phi_2 = -k,x \phi_{1,x}, \tag{A6}$$

where we used the fact that $\vec{\nabla} k(x)$ is orthogonal to $\nabla \phi_0$. The last equation already tells us that the perturbation theory is going to be problematic in the discontinuous perturbation case, since k_x is singular.

The boundary condition (BC) $P(h) = P_0$ becomes (to order λ^2)

$$\begin{aligned} \phi_0(h_0) &= P_0, \\ \phi_{0,y}(h_0)\overline{h_1} + \phi_1(h_0) &= 0, \\ \phi_{0,y}(h_0)\overline{h_2} + \phi_{1,y}(h_0)\overline{h_1} + \phi_2(h_0) &= 0. \end{aligned} \tag{A7}$$

Insertion of the previous equations in $\dot{h} = \text{const.}$ gives (again to order λ^2)

$$\begin{aligned} \dot{h}_0 &= -\overline{\kappa} \phi_{0,y}(h_0), \\ \dot{h}_i &= -\overline{\kappa}[\phi_{1,y}(h_0) + k(x)\phi_{0,y}(h_0)] = \text{const.} \\ \dot{h}_2 &= -\overline{\kappa}[\phi_{2,y}(h_0) + \phi_{1,yy}(h_0)\overline{h_1} - \phi_{1,x}(h_0)\overline{h_{1,x}} \\ &\quad + k(x)\phi_{1,y}(h_0)] = \text{const.} \end{aligned} \tag{A8}$$

We finally obtain the obvious results for ϕ_0:

$$\begin{cases} \nabla^2 \phi_0 = 0 \\ \phi_0(h_0) = P_0 \quad \text{(BC)} \end{cases} \Rightarrow \begin{cases} \phi_0 = \dfrac{P_0}{h_0} y \\ \dot{h}_0 = -\dfrac{\overline{K} \phi_0}{h_0} \end{cases}$$

getting again the average velocity V_s given in Eq. (2.14).

To solve the differential equations for $\overline{h_1}$ and $\overline{h_2}$ we consider the Fourier expansion of $\overline{h_1}(x)$, $k(x)$, and ϕ_1 (in normalized units)

$$\overline{h_1}(x) = \sum_{m=1}^{\infty} h_m \cos(\pi m x), \tag{A9}$$

$$k(x) = \sum_{m=1}^{\infty} k_m \cos(\pi m x), \tag{A10}$$

$$\phi_1(x,y) = \sum_{n=1}^{\infty} A_n \sinh(n\pi y)\cos(\pi n x). \tag{A11}$$

Equation (5.7) connects A_n and $\overline{h_1}$,

$$A_n = -\frac{P_0 \overline{h_1^n}}{h_0 \sinh(n\pi h_0)}. \tag{A12}$$

Using Eq. (5.8) and the fact that $\tanh(x)$ is one for large x, we get:

$$\overline{h_1^n} = \frac{k_n}{\pi n}, \tag{A13}$$

$$A_n = \frac{P_0 k_n}{h_0 \pi n \sinh(n\pi h_0)}. \tag{A14}$$

The calculation for $\overline{h}_2$ is more complicated. One uses Eqs. (5.6) and (5.7) to derive expressions for ϕ_2 and $\overline{h}_2$. After some calculation we get

$$\overline{h}_2^n = B_n + \frac{C_n + D_n}{2\pi n}, \tag{A15}$$

where the coefficients are given by

$$B_n = \sum_{l=1}^{\infty} \frac{(k_{n-l} + k_{n+l})k_l}{2\pi l}, \tag{A16}$$

$$C_n = \sum_{l=1}^{\infty} \frac{n-l}{l} k_{n-l}k_l + \frac{n+l}{l} k_{n+l}k_l, \tag{A17}$$

$$D_n = 2\sum_{l=1}^{\infty} k_{n-l}k_l. \tag{A18}$$

(A19)

For the case of the defect the natural choice for $k(x)$ is given by:

$$k(x) = \begin{cases} \beta\ \mathrm{sgn}(k_1 - k_2), & 0 < x < L(1-\beta)/2 \\ (1-\beta)\mathrm{sgn}(k_2 - k_1), & L(1-\beta)/2 < x < L(1+\beta)/2 \\ \beta\ \mathrm{sgn}(k_1 - k_2), & L(1+\beta)/2 < x < L. \end{cases}$$

Expanding $k(x)$, $\phi_1(x,y)$, and $\overline{h}_1(x)$ in Fourier series and inserting in Eq. (5.13), we obtain

$$\phi_1(x,y) = \frac{P_0}{\pi^2 h_0} \sum_{m=1}^{\infty} \frac{(-1)^m \sin(\beta m\pi)}{m^2} \frac{\sinh(2m\pi y)}{\sinh(2m\pi h_0)} \times \cos(2m\pi x) \tag{A20}$$

$$\overline{h}_1(x,\beta) = \frac{1}{\pi^2} \sum_{m=1}^{\infty} \frac{(-1)^{m+1}}{m^2} \sin(\beta m\pi)\cos(2m\pi x). \tag{A21}$$

Though the solution $\overline{h}_1$ is regular, it is interesting to note that the angle at the defects is always $\pi/2$. While this result is in accord with the cosine relation, it is not in accord with our initial assumption in the perturbation theory, that $\tan\theta(x)$ is small all along the front, Eq. (5.1).

When we try to calculate the second order term we get into more trouble. The gradients of $k(x)$ are not continuous, and therefore the corrections near the transition point will be discontinuous and not in accord with Eq. (5.20).

[1] M. Klman, *Points, Lines and Walls* (John Wiley and Sons, New York, 1983).

[2] M. C. Cross and P. C. Hohenberg, Rev. Mod. Phys. **65**, 851 (1993).

[3] J. Fineberg and V. Steinberg, Phys. Rev. Lett. **58**, 1332 (1987); E. Moses, J. Fineberg, and V. Steinberg, Phys. Rev. A **35**, 2757 (1987); I. Rehberg, S. Rasenat, and V. Steinberg, Phys. Rev. Lett. **62**, 756 (1989).

[4] M. Assenheimer and V. Steinberg, Nature (London) **367**, 345 (1994).

[5] R. Kapral and K. Showalter, in *Chemical Waves and Patterns* (Kluwer Academic Publishers, Dodrecht, 1995); A. Belmonte, Q. Ou-Yang, and J.-M. Flesselles, Europhys. Lett. **35**, 665 (1996).

[6] P. Coullet and J. Lega, Europhys. Lett. **7**, 511 (1988).

[7] N. D. Mermin, Rev. Mod. Phys. **51**, 591 (1979).

[8] P. G. Saffman and G. I. Taylor, Proc. R. Soc. London, Ser. A **245**, 155 (1958).

[9] R. Lenormand, E. Touboul, and C. Zarcone, J. Fluid Mech. **169**, 1165 (1988).

[10] J. Krug and P. Meakin, Phys. Rev. Lett. **66**, 703 (1991).

[11] O. Zik, E. Moses, Z. Olami, and I. Webman, Europhys. Lett. **38**, 509 (1997).

[12] J. F. Joanny and P. G. de Gennes, J. Chem. Phys. **81**, 552 (1984).

[13] D. Kandel, G. Gershinsky, D. Mukamel, and B. Derrida, Phys. Scr. **48**, XX (1993); D. Kandel and D. Mukamel, Europhys. Lett. **62**, 325 (1992).

[14] A. Marmur, J. Colloid Interface Sci. **124**, 301 (1988); A. Marmur, Adv. Colloid Interface Sci. **39**, 13 (1992). D. Danino, M.Sc. thesis, Department of Chemical Engineering, Technion-Israel Institute of Technology (1989).

[15] O. Zik, Physica A **224**, 338 (1996).

[16] M. Kardar, G. Parisi, and Y.-C. Zhang, Phys. Rev. Lett. **56**, 889 (1986).

[17] The existence of a maximal scale for a steady state solution is in fact obvious since the potential in this case should be written as $P(x,y) = \Sigma_k A_k \cos(kx)\sinh(ky) + P_0/H(t)y$. The minimal wavelength is defined by the minimal k in this sum which is finite. We assume in this approximation that there is one dominant wavelength.

[18] I. M. Hais and K. Macek, *Paper Chromatography* (Czechoslovac Academy of Sciences, 1963).